Semiconducting Carbon Nanotubes for Improved Efficiency and Thermal Stability of Polymer–Fullerene Solar Cells

Teddy Salim, Hang-Woo Lee, Lydia Helena Wong, Joon Hak Oh, Zhenan Bao, and Yeng Ming Lam**

The effects of the incorporation of semiconducting single-walled nanotubes (sc-SWNTs) with high purity on the bulk heterojunction (BHJ) organic solar cell (OSC) based on regioregular poly(3-hexylthiophene-2,5-diyl):[6,6]-phenyl-C_{61}-butyric acid methyl ester (rr-P3HT:PCBM) are reported for the first time. The sc-SWNTs induce the organization of the polymer phase, which is evident from the increase in crystallite size, the red-shifted absorption characteristics and the enhanced hole mobility. By incorporating sc-SWNTs, OSC with a power conversion efficiency (PCE) as high as 4% can be achieved, which is ≈8% higher than our best control device. A novel application of sc-SWNTs in improving the thermal stability of BHJ OSCs is also demonstrated. After heating at 150 °C for 9 h, it is observed that the thermal stability of rr-P3HT:PCBM devices improves by more than fivefold with inclusion of sc-SWNTs. The thermal stability enhancement is attributed to a more suppressed phase separation, as shown by the remarkable decrease in the formation of sizeable crystals, which in turn can be the outcome of a more controlled crystallization of the blend materials on the nanotubes.

1. Introduction

Solution-processable organic solar cells (OSCs) are promising in the realization of renewable, inexpensive, lightweight, and flexible solar energy conversion devices, potentially viable for large-area manufacturing.[1–3] Traditionally an OSC device consists of a photoactive bulk heterojunction (BHJ) layer of conjugated polymer as electron donor (D) and fullerene as electron acceptor (A), which is sandwiched between electrodes with different work functions. Tremendous improvement in power conversion efficiency (PCE) of BHJ-based OSC devices has been achieved over the past decade. Recently, the state-of-the-art PCE in excess of 9% has been reported for single-junction device.[4] A more encouraging PCE over 10% has also been demonstrated for OSC with tandem architecture.[5] In order to achieve OSC devices with high performance, it is crucial to optimize the blend morphology such that both donor and acceptor form interpenetrating bicontinuous nanoscale network favorable for both exciton dissociation and charge transport. There are a few approaches commonly employed to induce a more thermodynamically stable and optimally phase-separated morphology, e.g., thermal annealing,[6] solvent annealing,[7] solvent additive,[8–10] and the use of polymer nanostructures.[11,12]

The ternary OSC is an interesting concept to improve device performance.[13] Dopant materials with superior optical and electrical properties (e.g., complementary absorption spectra or higher charge-carrier mobility) are strategically incorporated into the polymer–fullerene blends. There are two main limitations in the design of ternary blend systems: 1) energy level compatibility between dopants and active materials, and 2) dopant dispersibility in the photoactive layer. A cascading alignment of the energy levels is preferred as it promotes both charge transfer at "guest–host" interfaces and charge transport to the respective D or A phase. The dopant materials should mix homogeneously with the active materials as aggregation may eventually affect device properties. Various types of dopants have been successfully applied in BHJ OSC devices, e.g., narrow bandgap materials,[14] dyes,[15] heavy metal complexes,[16] fullerene derivative,[17] and carbon nanostructures.[18–24]

Carbon nanotubes (CNTs), single-walled nanotubes (SWNTs) in particular, are promising constituents for ternary composites due to their ballistic charge transport, in addition to their good solution processability, high flexibility, and excellent mechanical and chemical stability.[25–27] The incorporation of both pristine and functionalized SWNTs has been reported to show performance enhancement in various polymer–fullerene solar cell devices.[18–20,28–30] On the other hand, there is also a growing effort in the fabrication of all-carbon solar cell devices.[31–33] The considerable interest in using CNTs for sustainable energy applications, along with their prospects and challenges, has been summarized in a few review articles.[34–37] To date, the reported

T. Salim, Dr. L. H. Wong, Prof. Y. M. Lam
School of Materials Science and Engineering
Nanyang Technological University
50 Nanyang Avenue
Singapore 639798, Singapore
E-mail: ymlam@ntu.edu.sg
Dr. H.-W. Lee, Prof. Z. Bao
Department of Chemical Engineering
Stanford University
Stanford, CA 94305, USA
E-mail: zbao@stanford.edu
Dr. J. H. Oh[+]
School of Nano-Bioscience and Chemical Engineering
Low Dimensional Carbon Materials Center
Ulsan National Institute of Science and Technology (UNIST)
Ulsan 689-798, Republic of Korea
[+]Present Address: Department of Chemical Engineering, Pohang University of Science and Technology (POSTECH), 77 Chungam-ro, Namgu, Pohang, Gyeongbuk 790-784, Republic of Korea

DOI: 10.1002/adfm.201503256

SWNTs used in ternary devices tend to be mixtures of both semiconducting (sc-) and metallic (m-) SWNTs. As BHJ dopants, m-SWNTs may have detrimental effects because: 1) they can contribute to device short-circuiting, 2) they can form recombination centers, and 3) they can shorten the lifetime of charge-carriers.[38,39] It is, therefore, highly desirable to remove m-SWNTs from the nanotube mixtures prior to their incorporation into ternary OSC devices. Abeygunasekara et al. obtained a better performance improvement for their BHJ OSC devices by removing some portion of the metallic nanotubes (95 wt% sc-SWNTs).[40]

Besides PCE, long-term thermal stability is another crucial factor to consider in terms of future commercialization. Since solar cells have to be continuously exposed to long hours of solar irradiation, the accumulated heat may effectively raise the operational temperature of the devices. Therefore, most BHJ OSCs traditionally have moderate to poor long-term thermal stability as a result of the relatively low glass-transition temperature (T_g) of the active materials, which could drive the evolution from an optimally nanoscale phase separated to a detrimental micro- (or even meso-) scale phase-separated morphology upon excessive heat exposure. The latter is usually associated with the formation of sizable crystals of donor and acceptor, which are much larger than exciton diffusion length (L_D) with a considerable concomitant reduction in the number of D/A interfaces. As expected, device performance inevitably deteriorates due to the heat-induced destruction of optimum blend morphology.

There are a few strategies to improve long-term thermal stability of polymer–fullerene solar cells: 1) incorporation of compatibilizers (functionalized polymers or block copolymers) to reduce interfacial tension between donor and acceptor phases,[41–46] 2) crosslinking of active materials,[47–52] 3) use of amorphous fullerene derivatives to substitute PCBM,[53–57] 4) reduction of polymer regioregularity,[58–60] and 5) utilization of active materials with high T_g.[61,62] The commonality of those approaches lies in the suppression of extensive molecular diffusion of the active materials. Nevertheless, most of the reported efforts to stabilize phase separation in BHJs involve nontrivial synthesis of new materials. Furthermore, there is always a trade-off effect in that the restriction of microscale phase separation may prevent the attainment of optimal bicontinuous nanomorphology. The introduction of the seemingly compatible novel materials may further require exhaustive optimization in terms of processing conditions (solvent choice, concentration and/or post-deposition treatment). As a result, the development of a more straightforward approach to achieve thermally stable morphology is necessary.

We have developed a simple method to sort sc-SWNTs with high purity by using regioregular poly(3-dodecylthiophene-2,5-diyl) (rr-P3DDT).[63] Resonant Raman scattering (RRS) measurement verified the complete removal of m-SWNTs. In this work, we demonstrate the application of highly pure sc-SWNTs as additives for BHJ based on regioregular poly(3-hexylthiophene-2,5-diyl):[6,6]-phenyl-C_{61}-butyric acid methyl ester (rr-P3HT:PCBM), the most widely studied BHJ for OSCs.[64,65] The extensive characterizations of the sorted sc-SWNTs are beyond the scope of this paper and can be found in our previous publication.[63] We found out that sc-SWNTs facilitated the nanostructuring of the blend layer, leading to improvement in photoabsorption and charge transport. The sorting polymer, which was present as a thin wrapping layer, did not pose any harmful effect on the device. In fact, PCE as high as 4% could be obtained with sc-SWNT incorporation. Very interestingly, the incorporated sc-SWNTs also acted as "cement" in restricting the movement of the blend active materials under long-term heat exposure. We correlated this with the templating effect of sc-SWNT in controlling the phase separation of both polymer and fullerene. Therefore, incorporation of sc-SWNTs acts as a simple yet effective novel approach to enhance thermal stability of rr-P3HT:PCBM BHJ OSC devices.

2. Results

Figure 1a shows an atomic force microscopy (AFM) image of the sorted high-pressure carbon monoxide (HiPCO) semiconducting single-walled nanotubes (sc-SWNTs). The nanotube length varies between 0.5 and 1 μm with diameter (d) range of 0.7–1 nm. The proportion of sc-SWNTs with larger diameters

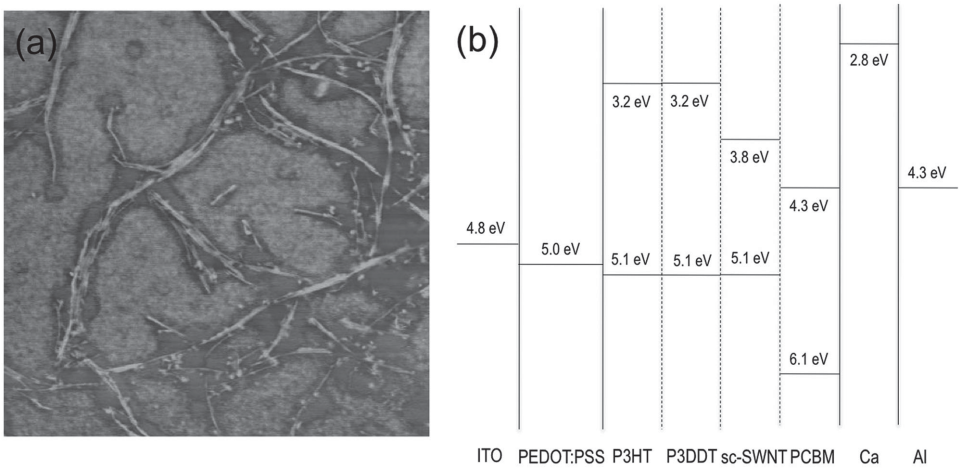

Figure 1. a) Tapping-mode AFM phase image of sc-SWNT deposited on Si substrate. The scan size is 5 μm × 5 μm. b) Energy-level diagram of the components in the OPV devices used in this study. The energy levels of sc-SWNT are estimated based on the transition energies of nanotube with $d \approx 1$ nm.[62].

($d \geq 1.1$ nm) also decreased after sorting. In addition, there is little aggregation/bundling observed among sc-SWNTs, as evidenced by well-resolved ultraviolet–visible–near infrared (UV–Vis–NIR) absorption peaks in NIR range (Figure S1, Supporting Information), implying outstanding nanotube dispersion.[63] Figure 1b depicts the orbital energy-level diagram of the respective components in the solar cell. A sc-SWNT typically exhibits inverse-dependence of energy band gap (E_g) on nanotube diameter. As our sorting approach yields nanotubes with nonmonodispersed diameters, a distribution of energy levels and heterogeneity of electronic properties of sc-SWNTs are expected. The conduction-band minimum (E_C) and valence-band maximum (E_V) of our sc-SWNTs are estimated to be ≈3.8 and ≈5.1 eV, respectively, based on the transition energies of nanotube with $d \approx 1$ nm.[66]

Incorporation of sc-SWNTs into the active layer gives rise to a few new heterojunctions: sc-SWNT/PCBM, rr-P3DDT/PCBM, rr-P3HT/rr-P3DDT, rr-P3HT/sc-SWNT, and rr-P3DDT/sc-SWNT. To ensure efficient dissociation of photogenerated excitons, which is one of the crucial steps in the operation of excitonic solar cells, staggered (type-II) interfacial energy alignment with positive band offsets is desirable. The E_V and E_C of sc-SWNT are higher than the highest occupied molecular orbital (HOMO) and lowest unoccupied molecular orbital (LUMO) of PCBM, respectively, resulting in positive valence band offset (ΔE_V) of 1 eV and conduction band offset (ΔE_C) of 0.5 eV at sc-SWNT/PCBM interface. The band offsets promote electron transfer from sc-SWNT to PCBM following exciton dissociation at the heterointerface. Due to considerable structural similarity between rr-P3DDT and rr-P3HT, it is expected that rr-P3DDT/PCBM heterojunction will possess similar electronic character to that of rr-P3HT/PCBM. The rr-P3DDT:PCBM system has been reported to exhibit photovoltaic properties, as shown by Yan et al., although it yielded a lower device performance as compared to rr-P3HT:PCBM due to the slight difference in mesoscopic morphology.[67] In our sorted sc-SWNTs, however, rr-P3DDT molecules form a more physically intimate contact with the nanotubes in the form of ordered supramolecular structures. This may in turn limit the intermolecular interaction between rr-P3DDT and PCBM, and hence, its contribution in the photoconversion process. The last type of heterojunction is polymer/nanotube (rr-P3AT/sc-SWNT) interface, which may also exhibit type-II behavior. By studying the photoluminescence excitation (PLE) spectra of polymer/sc-SWNT, Schuettfort et al. corroborated that type-II band alignment would be more feasible to manifest with sc-SWNTs with smaller diameters (or wider bandgaps), i.e., when the band offsets are energetically sufficient for exciton dissociation.[66,68] Stranks et al. have also discovered from femtosecond spectroscopic measurements that even small-diameter sc-SWNT with weight fraction as low as 1 wt% may allow efficient photon-to-charge conversion.[69] In this type of heterojunction, rr-P3AT and sc-SWNT expectedly act as electron donor (D) and electron acceptor (A), respectively. Nevertheless, as will be discussed later, this is not necessarily the case. In order to understand the influence of sc-SWNT addition, optical, morphological, structural, and electrical properties of rr-P3HT:PCBM bulk heterojunctions (BHJs) were investigated.

2.1. Optical Properties

Figure 2a shows the UV–vis absorption spectra of thermally treated polymer blends with various sc-SWNT concentrations, revealing an absorption feature with two peaks and two shoulders. The peak at 330 nm corresponds to PCBM absorption, while the peak (λ_{max}) at 520 nm and both vibronic shoulders at 580 nm and 610 nm (corresponding to 0–1 and 0–0 transitions, respectively) are absorption characteristics of rr-P3HT. Although rr-P3DDT/sc-SWNT hybrid nanostructures exhibit strong peaks between 500 and 600 nm (Figure S1, Supporting Information), they are expected to have minimum contribution in terms of blend absorption in the UV–vis region due to their low concentration. The corresponding absorption spectra of as-cast rr-P3HT:PCBM blends (Figure S2a, Supporting Information) exhibit a distinctly increasing bathochromic shift with an increase in sc-SWNT concentration. Even low sc-SWNT loading (0.1 wt%) could induce P3HT peak shift from 480 to 510 nm and prompt the emergence of more discernible vibronic shoulders, suggesting a more rigid structure of rr-P3HT molecules in the presence of nanotubes.[70] Nevertheless, the change in absorption spectra appears to saturate at higher sc-SWNT loadings. The role of CNT as nanostructuring template for conjugated polymers and its effects on their optical properties have been previously reported.[18,20,23,71–73] Conjugated polymers, e.g., regioregular polythiophene derivatives, interact noncovalently with nanotubes

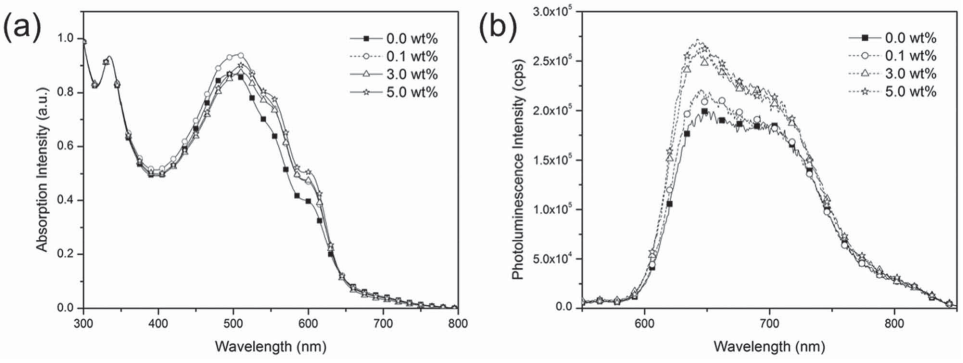

Figure 2. a) UV–vis absorption and b) normalized photoluminescence (PL) spectra of rr-P3HT:PCBM blends with different sc-SWNT concentrations. The samples were prepared on glass substrates and were subjected to thermal annealing at 150 °C for 30 min. The excitation wavelength (λ_{ex}) for the PL measurement is 520 nm.

via π–π stacking to form self-assembled wrapping layers. The polymer/nanotube hybrid nanostructures in turn induce molecular organization of the "free" polymer molecules in the blend. Unlike previous reports,[18,20,23] both wrapping and blend polymers are different in our system, i.e., rr-P3DDT and rr-P3HT, respectively. The observed extended π-conjugation length of rr-P3HT could be due to its direct interaction with either sc-SWNT and/or rr-P3DDT. The latter is more feasible to occur as the sc-SWNT/rr-P3DDT supramolecular structures may have fewer binding sites for rr-P3HT molecules. In addition, the stacking of rr-P3HT on rr-P3DDT could also be enhanced by both thiophene π–π interaction and alkyl side-group interaction.

On the contrary, the annealed rr-P3HT:PCBM blend exhibits only marginal red-shift with sc-SWNT incorporation. Thermal annealing above glass transition temperature (T_g) typically triggers molecular reorganization resulting in a more structured donor and acceptor phases, which is analogous to the effect of sc-SWNT-induced nanostructuring.[74] Consequently, the addition of sc-SWNT improves the blend absorptivity followed by modest refinement of the vibronic bands due to enhanced P3HT crystallinity. The slight increase in absorbance is expected to improve photon harvesting that may lead to better charge generation. The rr-P3HT:PCBM blends with higher sc-SWNT concentrations exhibit slightly more prominent shoulders at the expense of λ_{max}, which is a clear indication of increased interchain order or better blend crystallinity. However, this may not be an indication of a complete disordered-to-ordered domain transformation of rr-P3HT phase; instead, it could suggest either a thermally activated aggregation of crystalline P3HT phase or a mere reorganization of existing ordered polymer domains in the presence of the nanotubes, which may lead to a different type of nanostructuring of the polymer blend.

Photoluminescence (PL) measurement substantiates our previous claim that polymer phase aggregates upon sc-SWNT introduction. Figure 2b displays the normalized PL spectra of thermally annealed rr-P3HT:PCBM blends with various sc-SWNT concentrations. The spectra were normalized to the blend absorption. At excitation wavelength (λ_{ex}) of 520 nm, which corresponds to λ_{max} absorption of rr-P3HT, the polymer emission is expected to dominate the PL spectra. The PL peak at 650 nm and the shoulder at 700 nm correspond to the $S_1 \rightarrow S_0$, 0–0, and 0–1 transitions of rr-P3HT, respectively.[75] The shown spectra are the remnant of rr-P3HT emission, since fullerene molecules can efficiently quench the luminescence of donor polymer even at low concentrations. The presence of the rr-P3HT emission suggests a suboptimal rr-P3HT:PCBM blend morphology.[76] By increasing sc-SWNT concentration in the polymer blend, the PL of rr-P3HT:PCBM gradually enhances (or becoming less quenched) with no peak shift observed, similar to the observation made by Alley et al.[77] Our previous study on the PLE spectra of sc-SWNT sorted with rr-P3DDT reveals that the nanotubes do not exhibit significant PL below 900 nm;[63] therefore, the PL increase in rr-P3HT:PCBM blend could be attributed to decrease in rr-P3HT exciton quenching. Since PL is associated with the recombination of photogenerated excitons, PL quenching is indicative of the existence of alternative pathways for excitons besides radiative recombination, e.g., exciton dissociation followed by charge transfer from donor to acceptor at interfaces. The efficiency of PL quenching of a donor–acceptor blend depends on the amount of D/A heterojunctions available and the domain size of the active materials.[78–81] Both parameters are inversely related to each other, i.e., larger domain size indicates fewer interfaces, and vice versa. If the distance between polymer phase and fullerene phase becomes larger than the exciton diffusion length (L_D), more excitons will recombine radiatively before reaching the D/A interfaces, giving rise to an increase in PL intensity. The increase in emission of rr-P3HT:PCBM blend upon sc-SWNT incorporation suggests a decrease in the interface area between donor and acceptor and/or increased rr-P3HT domain size. In other words, sc-SWNTs modify the blend morphology and the size of rr-P3HT crystallites. Another explanation of the higher PL is the increase in effective π-conjugation length of rr-P3HT due to the aggregation onto the rigid sc-SWNTs, which gives rise to larger dipole strength, larger oscillatory strength, and shorter emission lifetime.[82–84] The relative PL intensity of the 0–0 and 0–1 vibronic peaks (I_{0-0}/I_{0-1}) can also be correlated with the degree of order of rr-P3HT in the blend. The values vary from 1.11, 1.13, 1.21, to 1.23 for the thermally annealed rr-P3HT:PCBM with 0, 0.1, 3, and 5 wt% of sc-SWNT, respectively. The increasing trend with sc-SWNT concentration implies that better ordering is achieved with more nanotubes. Similar observation of the effect of sc-SWNT can also be seen in the as-cast blends (Figure S2b, Supporting Information), with the main difference being remarkable enhancement in PL intensity even at sc-SWNT concentration as low as 0.1 wt%. This suggests that the structuring effect is more significant in the system with lower crytallinity. Therefore, our sorted sc-SWNTs not only increase the domain size but they also improve the degree of order of the polymer phase.

It is also worth pointing out that unlike previous reports showing PL quenching of rr-P3HT with the addition of sc-SWNT, usually associated with the formation of type II heterojunction, our finding implies that quenching is not always expected.[19,70,85,86] It is possible that SWNT used in the previous works still contained a substantial amount of metallic SWNTs (m-SWNT). By employing density functional theory (DFT) calculation, Kanai and Grossman demonstrated that quenching-like effect could arise from electron transfer either from the donor LUMO to the m-SWNT "mid-gap" electronic states or from the m-SWNT Fermi level to the donor HOMO.[87] Due to the absence of metallic nanotubes in our sorted system, m-SWNT-induced nonradiative recombination pathways are not expected to affect the emission of rr-P3HT in the active layer; hence, the PL results can be entirely interpreted based on morphological and structural changes of the blend. Interestingly, rr-P3HT PL was not significantly quenched by SWNTs. In terms of photovoltaic properties, the decrease in the amount of rr-P3HT/PCBM D/A interfaces resulting from the interaction between polymer and nanotube could potentially reduce the efficiency of exciton dissociation into free carriers. On the other hand, the slight enhancement in rr-P3HT order as induced by sc-SWNT may yield compensative effect with improvement in carrier transport.

2.2. Blend Morphology and Structural Properties

To further confirm the change in blend morphology, AFM measurement was performed on the blend samples. **Figure 3**

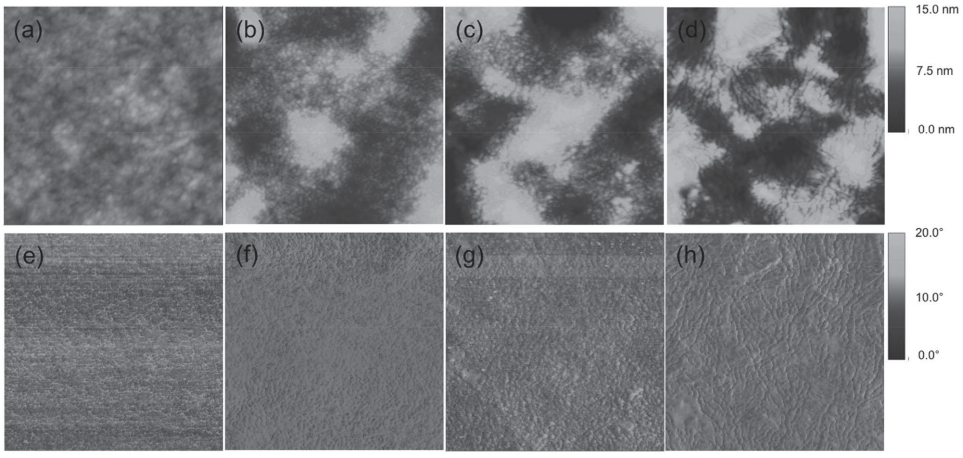

Figure 3. Tapping-mode AFM images of rr-P3HT:PCBM blends with different sc-SWNT concentrations: a,e) 0 wt%, b,f) 0.1 wt%, c,g) 3 wt%, and d,h) 5 wt%. The films were subjected to thermal annealing at 150 °C for 30 min. a–d) The top images correspond to topography images while e–h) the bottom ones correspond to the phase images. The scan size is 1 μm × 1 μm.

presents AFM topography and phase images (1 μm × 1 μm scan) of rr-P3HT:PCBM blends with different amount of sc-SWNTs. The corresponding 5 μm × 5 μm scan images are available in Figure S3, Supporting Information. Although AFM is usually employed to study surface characteristics, it has been reported that it is also capable of providing some information about the bulk phase separation.[88–90] The series of AFM images clearly shows the evolution of morphology change with increasing sc-SWNT concentration in the blend. The pure heat-treated rr-P3HT:PCBM (0 wt%) sample forms nanosized structures with estimated size of ≈15–20 nm. Addition of sc-SWNT increases the domatin size to ≈20–30 nm and 25–35 nm at sc-SWNT loading of 0.1 and 3 wt%, respectively. Interestingly, anisotropic elongated nanostructures with width of ≈25–30 nm and length of ≈100–250 nm were visible in the blend film with 5 wt% of sc-SWNT (Figure 3h). Furthermore, no tube-like structure could be seen on the blend surface of all samples, which is indicative of good nanotube dispersion as well as proper embedment of nanotube in polymer matrix. The analysis of 1 μm × 1 μm topography images yields root-mean-square roughness (σ_{RMS}) values of 0.8 nm (0 wt%), 2.3 nm (0.1 wt%), 3.9 nm (3 wt%), and 4.1 nm (5 wt%), revealing an increasing trend with increasing amount of sc-SWNT. The addition of sc-SWNT significantly roughens the blend film, as shown by the enhanced texturing of surface morphology. This is attributed to the growth of existing crystalline domains at the expense of the smaller ones.[74]

The structural change of the active materials, which is a manifestation of their interactions with sc-SWNTs, can be more straightforwardly probed from the grazing-incidence X-ray diffraction (GIXRD) patterns of as-cast rr-P3HT:PCBM:sc-SWNT blends as shown in **Figure 4**. In our previous study, we have observed self-assembly of rr-P3HT molecules into lamellae with edge-on configuration, i.e., in-plane π–π stacking of the

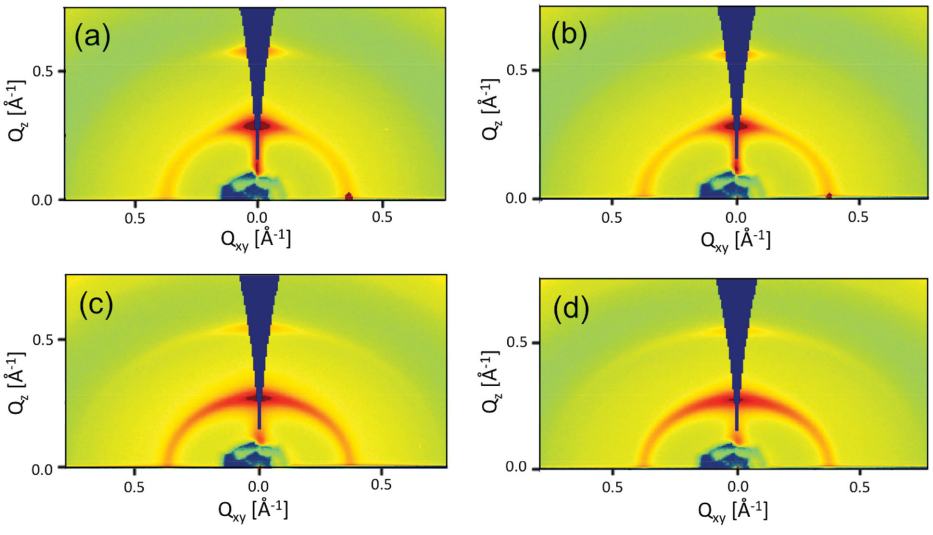

Figure 4. 2D GIXRD patterns for as-cast rr-P3HT:PCBM blends with different sc-SWNT concentrations: a) 0 wt%, b) 0.1 wt%, c) 3 wt%, and d) 5 wt%. The samples were prepared on Si substrates.

thiophene rings and out-of-plane stacking of the alkyl groups with respect to the substrate.[74] All blend samples exhibit distinct features of rr-P3HT with in-plane (100) and (200) peaks at q = 0.38 Å^{-1} and 0.75 Å^{-1}, respectively, and out-of-plane (010) peak at q = 1.65 Å^{-1}. In addition, there is an isotropic ring at q = 1.39 Å^{-1} corresponding to amorphous PCBM. By increasing sc-SWNT loading in the blend, it is noted that rr-P3HT domains become less oriented. At high sc-SWNT concentrations (3 wt% and 5 wt%), there is a decrease in the scattering intensity of (100) and (200) reflections in the out-of-plane direction, followed by the formation of more arching of the diffraction pattern (Figure 4c,d). This suggests that sc-SWNTs prompt a partial transformation of edge-on configuration into face-on configuration of rr-P3HT lamellae in the as-cast blends. As indicated by the improved optical absorption (Figure S2a, Supporting Information), the more isotropically ordered polymer phase should also have better crystallinity at higher sc-SWNT loading. Previously we proposed a geometric model of our rr-P3DDT/SWNT hybrid nanostructure based on modeling studies, which consists of a SWNT molecule wrapped by double-stranded rr-P3DDT layer with interdigitating dodecyl (DDT) groups.[63] The nanotubes tend to lie parallel to the substrate due to their high aspect ratios, which may then induce an in-plane stacking of the rr-P3HT molecules. As a result, there may be more perturbation of the orientation of the semicrystalline rr-P3HT domains in the samples with sc-SWNT. Subsequent heat treatment is expected to promote the aggregation among polymer molecules along the nanotubes. An increase in rr-P3HT crystallinity can also be seen in the as-cast blends with higher sc-SWNT loadings, evident from the stronger scattering intensity of (100) and (200) reflections. This is in strong agreement with the previous optical and morphological results. The stacking distance of rr-P3HT molecules within the lamellae does not change with sc-SWNT content. PCBM crystallinity could not be conclusively observed and compared, which is typically encountered for blends samples with comparable amount of donor and acceptor materials. Addition of sc-SWNT did not seem to change the amorphous morphology of PCBM. Next we will discuss the effects of improved degree of crystalline order of donor polymer on the electrical properties.

2.3. Electrical Properties

Space-charge-limited current (SCLC) method was employed to evaluate hole mobilities in the thermally annealed rr-P3HT:PCBM blends with various sc-SWNT concentrations. The measurement was done in dark on hole-only diode devices with the following configuration: ITO/PEDOT:PSS/rr-P3HT:PCBM:sc-SWNT/Au. Due to the similarity of device geometry to solar cell devices, the calculated charge-carrier mobilities are representative of vertical charge transport in the blend films, i.e., in the direction perpendicular to the electrodes. **Figure 5**a shows the double-logarithmic plot of

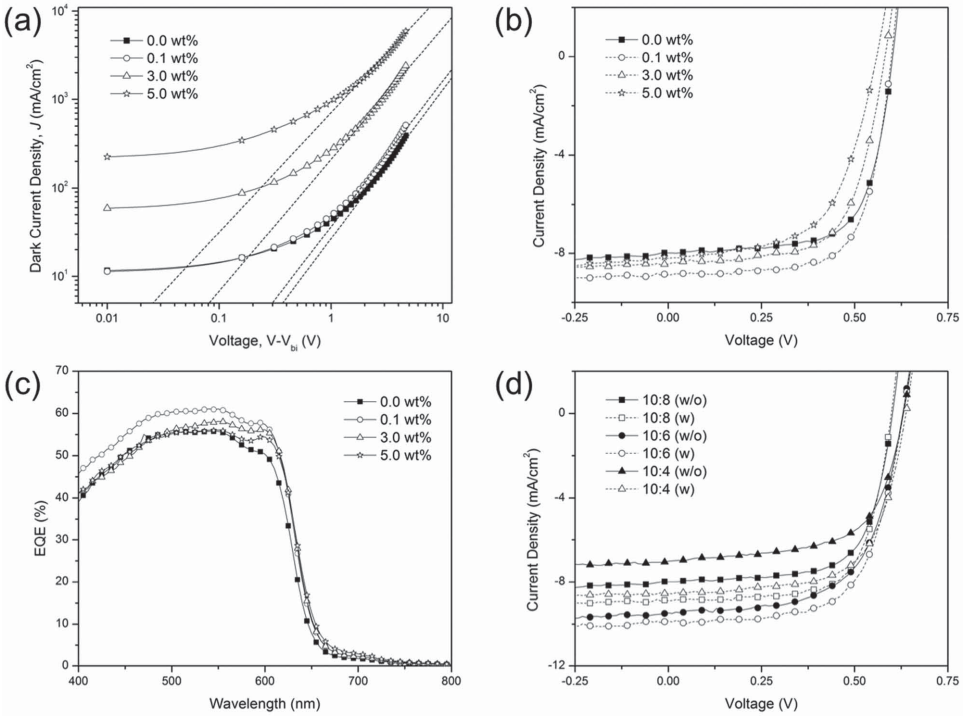

Figure 5. a) Dark current density–voltage (J_D–V) characteristics of hole-only rr-P3HT:PCBM devices with different sc-SWNT concentrations, fitted to the Mott–Gurney equation to extract the SCLC mobilities of the devices. The hole-only device structure is ITO/PEDOT:PSS/rr-P3HT:PCBM:sc-SWNT/Au. The dotted lines represent the fitting in the trap-free regime using the model. b) Current density–voltage (J–V) characteristics and c) EQE spectra of rr-P3HT:PCBM devices with different sc-SWNT concentrations. d) J–V characteristics of rr-P3HT:PCBM devices with different blend (D:A) ratios. The curves compare the devices with (w) and without (w/o) sc-SWNT loading. The sc-SWNT concentration is 0.1 wt%. The light J–V characteristics were measured under AM1.5G (100 mW cm^{-2}) illumination. The solar cell device structure is ITO/PEDOT:PSS/rr-P3HT:PCBM:sc-SWNT/Ca/Al. The devices were annealed at 150 °C for 30 min.

current density–voltage (J–V) characteristics of hole-only rr-P3HT:PCBM:sc-SWNT devices. Due to the low concentration (≤5 wt%) of sc-SWNT in the blends, all the J–V curves are essentially representative of the charge transport in the organic semiconductors; hence, they exhibit similar features. The J–V data were analyzed and fitted (linear least-square fit) to the modified Mott-Gurney equation,[91]

$$J = \frac{9}{8}\mu\varepsilon_r\varepsilon_0\frac{V^2}{d^3}\exp\left(\frac{0.89\gamma}{\sqrt{d}}\sqrt{V}\right) \quad (1)$$

where J is the current density, V is the applied voltage, which has been corrected for the built-in potential ($V = V_{appl}-V_{bi}$), μ is the zero-field charge-carrier mobility, ε_0 is the permittivity of free space (8.85×10^{-12} F m^{-1}), ε_r is the relative dielectric constant, d is the thickness of the active layer and γ is the field activation parameter. By using V_{bi} of 0.2 V and ε_r of 3.5, the calculated SCLC hole mobilities for thermally annealed rr-P3HT:PCBM:sc-SWNT films are 3.8×10^{-4} cm^2 V^{-1} s^{-1} (0 wt%), 4.8×10^{-4} cm^2 V^{-1} s^{-1} (0.1 wt%), 2.3×10^{-3} cm^2 V^{-1} s^{-1} (3 wt%) and 6.3×10^{-3} (5 wt%) cm^2 V^{-1} s^{-1}, revealing an increasing trend of hole mobility with sc-SWNT concentration. The hole mobility in the control device (0 wt%) is consistent with the typical values obtained from the other polythiophene blends.[92–94] At higher sc-SWNT concentrations (3 wt% and 5 wt%), we noted an improvement of approximately one order of magnitude in hole mobility. There are two possible reasons to the increased hole mobility: 1) hole transport via sc-SWNT, and 2) improved degree of order of rr-P3HT in the presence of sc-SWNT.

Due to their high one-dimensionality, CNTs are often characterized by their unique "ballistic" transport along their axes. We have previously reported high charge-carrier mobilities as high as 12 and 1.4 cm^2 V^{-1} s^{-1} based on sc-SWNT network thin-film transistor (TFT) and its corresponding wafer-scale transistor device, respectively.[63,95] On the other hand, charge transport in organic semiconductors predominantly depends on intermolecular and/or interchain hopping mechanism between localized electronic states. As long as charge-carriers from P3HT are transferred to SWNTs, e.g., from HOMO of rr-P3HT (–5.1 eV) to E_V of sc-SWNT (≈–5.1 eV, varies with chirality of the tube),[66] a more efficient charge transport could be acquired. The wrapping rr-P3DDT layer is expected to have minimum effect on the charge transfer between rr-P3HT and sc-SWNT because of its comparable HOMO level (–5.1 eV). Furthermore, due to the small thickness of rr-P3DDT layer (<1 nm), direct tunneling from rr-P3HT to sc-SWNT is also likely to take place.[96] Significant enhancement in charge transport has also been reportedly observed in other binary composites of conjugated polymers and CNTs.[19,22,97–100] Lee et al. have even demonstrated that selective enhancement in hole and electron transport of a nanocomposite could be achieved with *p*- or *n*-doping of the nanotubes, respectively.[22] Incorporation of SWNT could also decrease the dispersiveness of charge transport in rr-P3HT:PCBM matrix, as shown by Mallajosyula et al. from their impedance spectroscopy study, suggesting that SWNTs bridge the polymer molecules and induce the formation of better-percolated pathways in the polymer blend.[101] In addition, the purity of sc-SWNT may also affect the charge transport properties in the active layer. Liu et al. observed an increase in bimolecular recombination when more unsorted SWNTs were introduced into rr-P3HT:PCBM blends.[38] They attributed the reduced device performance at higher SWNT concentrations to the abundant m-SWNT, which promotes transfer of holes in rr-P3HT phase and electrons in PCBM phase to the charge-quenching "mid-gap" states of m-SWNT. However, excessive amount of sc-SWNT may also promote electron transfer from PCBM into nanotubes, resulting in bimolecular recombination with the existing holes. Such detrimental impacts with increasing SWNT loading were not observed in our system due to the high purity of the sorted sc-SWNT.

As an outcome of sc-SWNT-induced nanostructuring, the increased degree of order or rr-P3HT phase, which is in favorable agreement with the previous optical, morphological, and structural measurement results, is expected to have better interchain charge transport within the crystalline rr-P3HT domains. The charge carriers can travel longer distances in larger domains. The increase in domain size tends to be accompanied by a decrease in the number of grain boundaries. The higher mobility at higher sc-SWNT concentrations could also derive from significantly fewer grain boundaries in rr-P3HT:PCBM layer. This in turn reduces the number of charge carrier trapping defects localized at the grain boundaries, leading to enhanced charge transport across the domains.[102]

To confirm the efficacy of our SWNT selective sorting method, we performed a comparative device study with different types of SWNTs: sorted (sc-SWNT) and crude/unsorted (c-SWNT). To further aggravate the effects of m-SWNTs, thinner films (≈90 nm) were deliberately prepared and no electron-blocking layer (EBL) was used. The device configuration is ITO/PEDOT:PSS/rr-P3HT:PCBM:SWNT/Al with SWNT loading of 1 wt%. The dark and light J–V characteristics of the devices are shown in Figure S4 (Supporting Information), while the data are summarized in Table S1 (Supporting Information). Under AM1.5G (100 mW cm^{-2}) illumination, the as-cast rr-P3HT:PCBM device without thermal annealing exhibits poor performance with short-circuit current density (J_{SC}) of 3.12 mA cm^{-2}, open-circuit voltage (V_{OC}) of 0.692 V, fill factor (FF) of 0.35, and PCE of 0.76%. Addition of sc-SWNT significantly improves the device performance by almost threefold, largely due to increased J_{SC} and FF with slightly decreased V_{OC}. As discussed earlier, sc-SWNTs induce nanostructuring on rr-P3HT phase leading to improved blend absorption and charge transport. On the contrary, severe device degradation was observed following c-SWNT incorporation into rr-P3HT:PCBM devices. The noticeably low V_{OC} of 0.122 V contributes to the lowering of PCE to 0.13%. A similar trend was also seen in the heat-treated rr-P3HT:PCBM devices. Thermal annealing at 150 °C for 20 min results in an increase in both J_{SC} and FF, resulting in improved PCE to 2.74%. The thermal-driven molecular self-assembly prompts stronger intermolecular interactions among rr-P3HT chains, which results in the formation of crystalline domains. The inclusion of sc-SWNTs in the heat-treated device is also expected to further reorganize the ordered phases. Consequently, a much higher PCE of 3.40% could be obtained, i.e., about 25% higher than the device without any sc-SWNTs. An equivalent detrimental effect was still observed from the

heat-treated device upon c-SWNT incorporation, in which both V_{OC} and FF suffer remarkable drop. In the end, a low PCE of 1.27% was obtained for the thermally annealed device when the unsorted SWNT was used. Evidently, sc-SWNT and c-SWNT have opposite effects on device performance at 1 wt% loading. This comparative study also verifies that our sorting methodology is effective in removing harmful m-SWNTs as m-SWNTs contribute to device short-circuiting and poor shunting if they form percolating path connecting both electrodes.[19] This could be further worsened by the high aspect ratio of SWNTs (≥0.5 μm in length) in comparison to the thin active layers (<100 nm). As mentioned earlier, the continuous "mid-gap" states of m-SWNTs favor the formation of trapping and recombination centers. This could in turn increase bimolecular recombination and lower the short-circuit current.[38] In the following discussion, we will discuss the effect of sc-SWNT concentration on the device performance.

Figure 5b shows the *J*–*V* characteristics of rr-P3HT:PCBM devices incorporated with different amount of sc-SWNTs under AM1.5G illumination. The samples correspond to films with thickness of ≈200 nm with device configuration of ITO/PEDOT:PSS/rr-P3HT:PCBM:sc-SWNT/Ca/Al. The corresponding summary of the device performances is presented in **Table 1**. The thermally annealed rr-P3HT:PCBM control device (0 wt%) demonstrates high performance with J_{SC} of 7.97 mA cm^{-2}, V_{OC} of 0.61 V, FF of 0.68 and PCE of 3.30%. A better performing device with PCE of 3.54% was obtained with incorporation of 0.1% sc-SWNT. The device improvement is attributed to an increase in both J_{SC} and FF, similar to the case of thinner rr-P3HT:PCBM devices. The higher J_{SC} is attributed to improved blend absorption as well as a more efficient hole transport, both of which are the manifestation of enhanced π–π interactions among rr-P3HT molecules, which leads to the formation of crystallite domains with comparable size to L_D. It is noted that the plausible decrease in exciton dissociation, evident from the decrease in PL quenching and the formation of larger domains as observed from AFM, does not impose any notable consequences on the device performance at low sc-SWNT concentration. There is only slight change observed on both series resistance (R_s) and shunt resistance (R_{sh}) after sc-SWNT inclusion. Here, we need to emphasize that the improvement observed upon sc-SWNT incorporation is with reference to a superior control device (PCE > 3%). Although the other groups have reported similar performance enhancement by using CNTs as additives, substandard control devices (PCE < 3%) with poor quality of rr-P3HT and/or unoptimized blend morphology were often employed as baseline instead.[18,19,23,24,28,29,38] Our results clearly demonstrate that sc-SWNTs could still boost the performance of efficient OSC devices. Subsequent increase of nanotube loading to 5 wt% further reduces the device PCE to as low as 2.65%. The J_{SC} also drops from a peak at 8.76 to 8.11 mA cm^{-2}, while FF decreases from 0.68 to 0.59. The J_{SC} trend is in good agreement with that of the external quantum efficiency (EQE), presented in Figure 5c. The integration of EQE spectra yields comparable J_{SC} within ±5% variation. A monotonic decrease in V_{OC} was also observed with sc-SWNT concentration. The negative trend of V_{OC} correlates well with the increase in dark current density from the following relationship,

$$V_{OC} \approx n\frac{kT}{q}\ln\left(\frac{J_{SC}}{J_0}\right) \quad (2)$$

where n is the diode ideality factor, k is the Boltzmann constant, T is the temperature, q is the elementary charge (1.6×10^{-19} C) and J_0 is reverse saturation current density. The J_0, which shows an increasing trend in the dark semilog *J*–*V* plots (Figure S5, Supporting Information), is inversely proportional to the V_{OC}. The higher J_0 can be explained in terms of the upward-shift of HOMO level of rr-P3HT, which renders a more efficient charge transfer from the HOMO level of the donor to the charge-transfer (CT) state at the donor–acceptor interface. The electronic shift itself is induced by increased π–π interactions as a result of the increased ordering discussed earlier, as confirmed by Tsoi et al. from ultraviolet X-ray photoelectron spectroscopy (UPS) measurement.[103] The low V_{OC} at high sc-SWNT concentrations is not attributed to the V_{OC} reduction to the formation of shunting pathways since all devices demonstrate similar R_{sh}. The lack of m-SWNT in our sorted system, which has previously demonstrated excellent TFT on/off current ratio (I_{on}/I_{off}) of ≈10^{-6}, justifies the comparable R_{sh} values across the devices.[63] The diminished device performance is also suggestive of either a more enhanced exciton recombination possibly due to charge transfer to the sc-SWNTs as a

Table 1. Summary of performance parameters of OPV devices with sc-SWNTs. The device configuration is ITO/PEDOT:PSS/rr-P3HT:PCBM:sc-SWNT/Ca/Al. The measurement was done under AM1.5G illumination (100 mW cm^{-2}). The blend films were subjected to thermal annealing at 150 °C for 30 min before cathode (Ca/Al) deposition.

D:A ratio	sc-SWNT [wt%]	J_{SC} [mA cm^{-2}][a)]	V_{OC} [V][a)]	FF[a)]	PCE [%][a)]	R_s [Ω cm^2]	R_{sh} [Ω cm^2]
10:8	0.0	7.97 [0.08]	0.61 [0.00]	0.68 [0.01]	3.30 [0.04]	2.0	8.1×10^2
	0.1	8.76 [0.12]	0.60 [0.01]	0.68 [0.02]	3.54 [0.10]	2.1	1.2×10^3
	3.0	8.37 [0.03]	0.58 [0.00]	0.64 [0.00]	3.12 [0.05]	3.4	7.9×10^2
	5.0	8.11 [0.11]	0.56 [0.00]	0.59 [0.01]	2.65 [0.05]	4.0	1.0×10^3
10:6	0.0	9.56 [0.06]	0.63 [0.00]	0.61 [0.01]	3.69 [0.03]	3.1	5.5×10^2
	0.1	9.91 [0.17]	0.63 [0.01]	0.64 [0.01]	3.98 [0.03]	3.3	1.8×10^3
10:4	0.0	6.96 [0.08]	0.64 [0.00]	0.63 [0.00]	2.79 [0.01]	2.3	7.6×10^2
	0.1	8.41 [0.09]	0.64 [0.01]	0.65 [0.01]	3.51 [0.02]	2.8	1.6×10^3

[a)]The bracketed figures denote the corresponding standard deviations (SD).

result of increased domain size with more sc-SWNTs or a less efficient exciton dissociation due to decreased rr-P3HT/PCBM interface area. Both of the above effects may have substantially compromised the merit of increased hole transport with more sc-SWNTs. In addition, the decrease in FF at high sc-SWNT loading implies an imbalanced charge transport between electrons and holes in the devices.[104] This study suggests that it is important to carefully control the sc-SWNT amount in BHJ. It is necessary to optimize the accumulative benefits in terms of photon harvesting, exciton splitting, and charge transport.

In addition to optimizing sc-SWNT concentration in the active layer, we also investigated the effects of donor:acceptor (D:A) ratio. Both *J*–*V* characteristics under AM1.5G illumination and summary of the corresponding device performance are presented in Figure 5d and Table 1, respectively. Without any sc-SWNT incorporation, the best rr-P3HT:PCBM device was obtained with D:A ratio of 10:6, showing ≈15% improvement in performance compared to that with D:A = 10:8 with J_{SC} of 9.56 mA cm^{-2}, V_{OC} of 0.63 V, FF of 0.61 and PCE of 3.69%. Further lowering of PCBM content significantly deteriorates the PCE to 2.79%. The optimum rr-P3HT:PCBM weight ratio is often reported to be 1:1, which differs from our observation. Nevertheless, there are reportedly "anomalies" observed associated with better-optimized blend morphologies at low PCBM concentrations.[105,106] The variation in optimum D:A ratio depends on both blend processing conditions and active materials, i.e., rr-P3HT could be different in terms of molecular weight (M_W), regioregularity (%RR) and polydispersity (PDI). A marginal device enhancement of ≈8% could still be observed on rr-P3HT:PCBM (10:6) device upon the direct addition of 0.1 wt% sc-SWNT with J_{SC} of 9.91 mA cm^{-2}, V_{OC} of 0.63 V, FF of 0.64, and PCE of 3.98%. Analogous increase in both J_{SC} and FF to those in 10:8 blend suggests that the device improvement should come from sc-SWNT-induced nanostructuring. The 10:4 rr-P3HT:PCBM device experiences a more significant increase in PCE from 2.79% to 3.51% (≈46%). The influence of sc-SWNTs appears to be more prominent in BHJ systems with suboptimal performance, suggesting their application as dopants to fine-tune the BHJ morphology for the less efficient OSC devices.

2.4. Thermal Properties

The evolution of performance parameters (J_{SC}, FF, $V_{OC,}$ and PCE) of rr-P3HT:PCBM (no sc-SWNT) and rr-P3HT:PCBM:sc-SWNT (with sc-SWNT) devices as a function of annealing time is presented in Figure S6 (Supporting Information). The films were heat treated on a hotplate at 150 °C for various periods in N_2 glovebox prior to deposition of Ca/Al electrode. The parameters are normalized to their respective starting values at 30 min annealing. The corresponding summary of the device characteristics is provided in Table S2 (Supporting Information). As shown before, the employment of sc-SWNTs improves device performance, i.e., from 3.83% to 3.97%. It can be observed that rr-P3HT:PCBM suffers significant photocurrent loss (>15%) after 9 h annealing. On the contrary, the ternary device with sc-SWNTs exhibits negligible degradation in J_{SC} (<0.5%). The FF trend agreeably complies with the temporal behavior of the photocurrent. In the presence of nanotubes, FF remains unchanged, while a decrease of as much as 10% can be seen in the pristine device. Both types of devices do not show any significant change in V_{OC}.

The decay on both J_{SC} and FF in rr-P3HT:PCBM device is the result of a more severe phase separation of BHJ active materials, which in turn promotes considerable exciton recombination, inefficient charge generation as well as charge collection by electrodes (due to surface roughening). As discussed below, sc-SWNTs are capable of restricting severe crystallization of polymer and/or fullerene molecules. Consequently, thermally stable rr-P3HT:PCBM device (<5% PCE reduction) could be achieved with sc-SWNT incorporation, while the one without any nanotube suffers from a more serious degradation (>25% PCE reduction). Although a period of 9 h is arguably short for a proper thermal stability testing, it is evident from this study that there is a dramatic improvement in BHJ thermal stability in the presence of sc-SWNTs.

The morphology of both types of films was examined to gain further insight into the difference in thermal stability of the corresponding devices. **Figure 6** shows optical microscope images obtained from rr-P3HT:PCBM blend films with and without the incorporation of 0.1 wt% of sc-SWNTs. Thermal annealing at 150 °C for 0.5 h prompts the emergence of a small number of needle-like PCBM crystals in both binary and ternary blends, which has been observed in previous reports.[45,47,50,56,59] After 5 h of annealing, there are much more PCBM needle-like domains emerging in rr-P3HT:PCBM (Figure 6b) as compared to rr-P3HT:PCBM:sc-SWNT (Figure 6e). The formation of the needle-like structures becomes more severe in the pristine polymer blend after 9 h of annealing (Figure 6c). The dramatic increase in the coverage of PCBM needles on the blend surface elucidates the thermal instability of the rr-P3HT:PCBM solar cell device. Under intensive annealing conditions, polymer phase undergoes further crystallization, while fullerene tends to diffuse out of the polymer matrix, nucleate and grow into 1D aggregates.[56] The presence of nanotubes suggestively inhibits such progressive phase separation between rr-P3HT and PCBM. Interestingly, the PCBM needles also tend to be longer in the ternary blend (150–250 μm) than in the binary blend (40–100 μm). This indicates that the presence of sc-SWNTs may suppress the formation of many small fullerene crystals; instead only a few larger crystals can be found. It is possible that due to the interactions of PCBM and rr-P3HT with sc-SWNTs, the addition of the sc-SWNT suppressed the aggregation of PCBM and rr-P3HT by "holding" them in place. Chaudhary et al. have also proposed the preferential aggregation of PCBM on nanotube in a ternary blend system as a possible reason to the observed change in PL lifetime.[107] Likewise, rr-P3HT also has preferential interaction with sc-SWNTs, as described in the previous section. Since the major morphological difference observed was the reduction of overall PCBM crystallization, the improved device thermal stability is therefore attributed to mainly the suppression of PCBM crystallization due to PCBM/sc-SWNT interactions.

To probe our hypothesis that the thermal stability enhancement in rr-P3HT:PCBM blends is attributed to the interaction of PCBM with sc-SWNT, it is imperative to examine the organization of the fullerene molecules in the presence of sc-SWNTs.

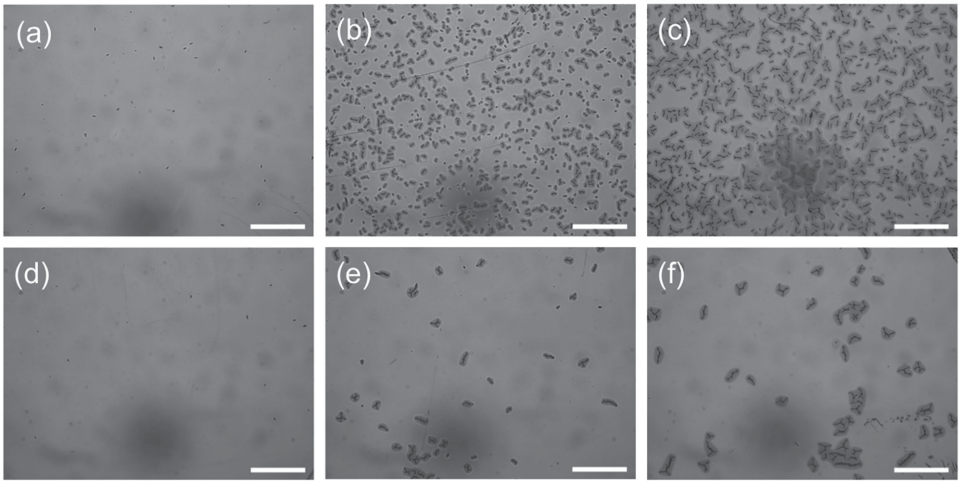

Figure 6. Optical microscope images of rr-P3HT:PCBM blends a–c) without and d–f) with sc-SWNT. The samples were prepared on ITO/PEDOT:PSS substrates and were subjected to thermal annealing at 150 °C for: a,d) 0.5 h, b,e) 5 h, and c,f) 9 h. The scale bar indicates length of 800 μm.

We performed GIXRD measurements on binary PCBM:sc-SWNT samples without rr-P3HT to examine whether the presence of sc-SWNT induces crystallization of PCBM. The samples were prepared by spin-coating PCBM solutions (50 mg mL^{-1} in *o*-DCB) at 800 rpm on Si substrates. The sc-SWNT loading percentage in the binary solutions was defined as weight ratio between sc-SWNT and total fullerene–nanotube composite. GIXRD images of thermally annealed PCBM films with various sc-SWNT concentrations are shown in **Figure 7**. The corresponding patterns of the as-cast binary blends are displayed in Figure S7, Supporting Information. The as-cast PCBM film shows a few isotropic rings at q = 0.71, 1.39, and 2.04 $Å^{-1}$. The fact that the diffraction rings are indistinct and broad implies that PCBM is in amorphous state and that the crystallite size is very small. By increasing sc-SWNT amount, an increase in the scattering intensity of the isotropic rings could be observed. The strongest reflections were noted in the PCBM sample with 5 wt% sc-SWNT (Figure S7d, Supporting Information). The presence of the more distinct isotropic rings is indicative of isotropic PCBM crystallization. Apart from crystallinity enhancement, the presence of sc-SWNTs was not found to induce any preferred crystal orientation. This indicates that fullerene molecules cluster on sc-SWNT. The GIXRD measurement of the heat-treated PCBM:sc-SWNT samples provides more evidence of sc-SWNTs acting as nucleating sites. Heat treatment promotes molecular mobility that leads to the cold crystallization of PCBM, i.e., crystallization above glass-transition temperature (T_g) and below melting temperature (T_m). The formation of a sharp diffraction peaks could be observed in the PCBM film upon heating to 150 °C (Figure 7a), which are associated with preferentially oriented PCBM crystallites relative to the substrate.[74] Incorporation of sc-SWNT at low concentration (0.1 wt%) does not induce any significant change in the scattering characteristics (Figure 7b). However, at higher sc-SWNT

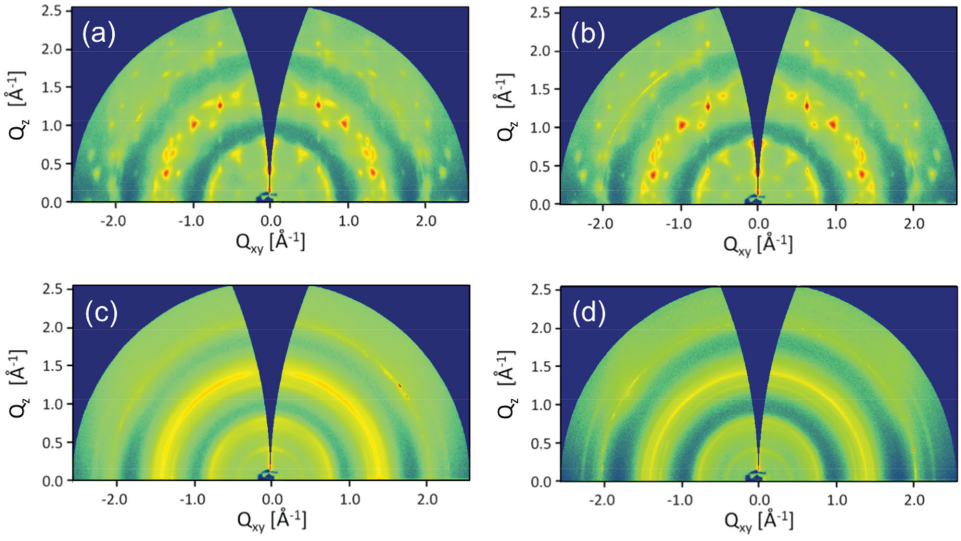

Figure 7. 2D GIXRD patterns for PCBM films with different sc-SWNT concentrations: a) 0 wt%, b) 0.1 wt%, c) 3 wt%, and d) 5 wt%. The samples were cast on Si substrates and were annealed at 150 °C for 0.5 h.

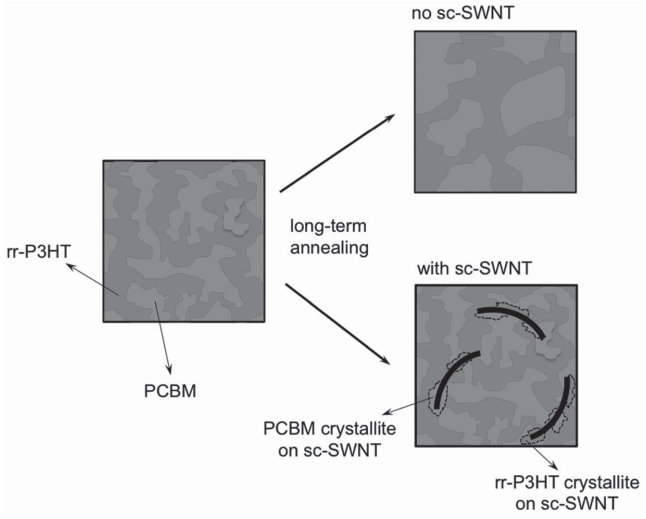

Figure 8. Proposed schematics on the effect of sc-SWNT on morphological stability of rr-P3HT:PCBM BHJ under long-term heat treatment.

loadings (3 wt% and 5 wt%), no sharp diffraction peaks were observed by thermal annealing, instead only weak sharp isotropic rings were observed (Figure 7c,d). This suggests that the nanotube tends to inhibit strong crystallization of PCBM when annealed above the cold-crystallization temperature (T_{cc}). It was also observed that PCBM crystallization in the films with 3 wt% and 5 wt% sc-SWNTs took place at lower temperatures (≤120 °C). The lowering of T_{cc} is a result of decreased energy barrier for crystallization, which is an indication of the increase in nucleating sites.

Based on the above results, we propose a mechanism on how the morphological thermal stability of rr-P3HT:PCBM BHJ can be enhanced with sc-SWNT incorporation, schematics of which are shown in **Figure 8**. Essentially, a spin-coated polymer blend experiences a fast-drying process that results in the formation of metastable morphology. Upon thermal annealing treatment, thermodynamically driven molecular diffusion triggers large-scale phase separation, which can be identified from the increased size of polymer and fullerene crystallites in the blend. In the presence of sc-SWNTs, however, the phase separation is suppressed since both polymer and fullerene molecules prefer to interact with the sc-SWNTs and nucleate heterogeneously on nanotubes.

3. Discussion

Thermal annealing under optimal conditions drives molecular reorganization of donor and acceptor molecules in order to attain a more thermodynamically stable state. In rr-P3HT:PCBM system, heat treatment usually results in more ordered donor and acceptor phases, represented by the appearance of nanocrystalline domains. Our study reveals that hybrid polymer/nanotube nanostructures could promote grain growth of the crystalline phases in the blend, which is likely to be a manifestation of the intermolecular interaction of rr-P3HT with sc-SWNT and/or rr-P3DDT "sheath." Singh et al. also observed similar phenomenon under electron microscopy, in which case semicrystalline P3HT phase formed surrounding the nanotube region in the composite film.[73] The emergence of the anisotropic structures also suggests a preferential alignment of ordered phases along the nanotubes during thermal annealing. The variation in domain size of the crystalline phases is expected to influence the efficiency of photovoltaic processes in the BHJ. The exciton diffusion length (L_D) in conjugated polymers is typically in the range of 5–15 nm.[108–111] PCBM has also been reported to have short diffusion lengths of ≈5 nm.[112,113] Excitons generated at a distance larger than L_D from D/A heterojunction tend to recombine before dissociating into free charges at the interface. The rr-P3HT:PCBM (0 wt%) blend is expected to have the most efficient exciton dissociation because its domain size is compatible with L_D. Nevertheless, Wang et al. proposed that excitons with L_D shorter than the domain size could still reach the interface via delocalization mechanism instead of diffusion, which loosens up the domain size restriction imposed based on L_D requirement.[111] Therefore the nanotube-incorporated blend samples with larger crystalline domains may suffer less from exciton recombination. On the other hand, the improved π-conjugation length within the domain may also promote an efficient charge transport. Due to the trade-off between exciton dissociation and charge transport, the loading of sc-SWNT in the blend has to be carefully controlled in order to achieve optimal device performance.

The incorporated sc-SWNTs have a few roles in the energy conversion processes in rr-P3HT:PCBM devices. In the first step of photon absorption by the photoactive layer, the inclusion of sc-SWNTs is expected to complement photon harvesting in the near-infrared (NIR) region (Figure S1, Supporting Information). In fact, we have previously demonstrated photovoltaic characteristics of sc-SWNT/C_{60} with NIR (≥800 nm) illumination.[32] However, the improvement associated with direct absorption of sc-SWNTs is insignificant due to their low concentration in the blend in this case. Indirectly, sc-SWNTs are capable of ameliorating the characteristic absorption of rr-P3HT resulting in red-shifted spectra with stronger absorptivity. In the second photoconversion step, the photogenerated excitons diffuse and get dissociated at heterointerfaces. As described earlier, the addition of sc-SWNTs generates a few heterojunctions with the existing active materials. As sc-SWNTs are surrounded by conjugated polymers and fullerenes in the blend, it is crucial to probe whether holes or electrons are to be transferred into sc-SWNTs. Most of the previous reports identified CNTs as *n*-type materials (electron acceptors).[19,114–117] It is possible for electron transfer from rr-P3HT to sc-SWNTs due to their low lying LUMOs. It is also possible for a direct hole transfer from the HOMO of polymer phase to the E_V of sc-SWNT due to the shallow E_V at sc-SWNTs.[97] On the other hand, sc-SWNT/PCBM heterojunctions are more likely to generate holes in sc-SWNT phase and electrons in PCBM phase. The opposing effect of sc-SWNT can be indirectly observed in the increased remnant PL of rr-P3HT. The lack of PL quenching in our system suggests that exciton dissociation becomes less efficient in the presence of sc-SWNTs, likely to be attributed by the increase in the size of crystalline domains. The final step of photoconversion deals with charge transport to the respective electrodes. There are two ways sc-SWNTs can contribute to the improved charge transport: 1) direct via formation of ballistic percolation pathways,

and 2) indirect via crystallinity enhancement of active materials. The intrinsic mobility of sc-SWNTs is exceptionally high in the order of $\approx 10^4$ cm^2 V^{-1} s^{-1}.[118,119] Nevertheless, as pointed earlier, the nature of sc-SWNT as *p*- or *n*-type material in a blend system thus far remains controversial. Having either electron-donating or electron-accepting sc-SWNTs can be detrimental since it increases the chance of charge recombination when holes and electrons are transferred into the same SWNT. The polymer layer also shields the nanotubes from being in direct contact with electron-transporting PCBM, making it more difficult to transfer electrons from sc-SWNTs to PCBM. Therefore, having a large percentage of sc-SWNTs may result in degradation to the device performance. On the other hand, with proper concentration, sc-SWNTs can prompt the nanostructuring of rr-P3HT phase, resulting in enhancement of hole mobility. Therefore, enhancement in device performance could only be achieved upon addition of proper amount of sc-SWNTs.

Here, we have also shown that sc-SWNT has the potential in improving long-term thermal stability of polymer–fullerene solar cells. This is related to the function of the nanotube as a morphological anticoagulant agent. This approach is straightforward since it does not involve any sophisticated synthesis step. Besides, the inherent characteristics of sc-SWNT can simultaneously enhance the device performance, yielding a dual functionality of sc-SWNT in BHJ OSCs. Nevertheless, the system still needs further optimization in terms of nanotube loading by considering maximum improvement in both performance and stability. Furthermore, the smaller-diameter HiPCO SWNTs, which are more susceptible to ultrasonic damage, can also be substituted with the larger-diameter arc-discharged SWNTs.[120] At last, it is also desirable to employ SWNTs with quasi-monodispersed diameters to minimize possible device variation attributed by diameter-dependent variables.

4. Conclusion

In summary, we have shown the first application of highly pure sc-SWNTs for rr-P3HT:PCBM BHJ OSC. Upon increasing the amount of sc-SWNTs in the blend, the domain size increases, leading to bathochromic shift in polymer absorption and higher hole mobility. This is suggestive of a more enhanced polymer interaction in the presence of sc-SWNTs. However, the larger crystallite size also reduces the number of interfaces available for exciton dissociation. Hence, the loading of sc-SWNTs in BHJ has to be carefully controlled to balance both effects. In terms of device performance, incorporation of sc-SWNTs increases both J_{SC} and FF, leading to PCE of 3.98% compared to 3.69% without addition of sc-SWNTs. On the other hand, the addition of unsorted SWNTs of comparable concentration significantly reduces the PCE due to the detrimental m-SWNTs present in the blend. It is also observed that sc-SWNTs can suppress excessive phase separation in rr-P3HT:PCBM BHJ, resulting in thermal stability improvement of more than five-fold as compared to the blend without any sc-SWNT. The formation of micron-sized PCBM needles upon intensive heat treatment is greatly suppressed in the presence of sc-SWNTs. We propose that sc-SWNTs act as nucleating sites for PCBM, which is evident from the improved PCBM scattering as well as reduction in cold crystallization temperature of PCBM. Incorporation of sc-SWNTs serves as a simple yet effective method to improve both device performance and thermal stability of BHJ-based OSC devices. Future work will investigate the use of sc-SWNTs as an additive for stabilizing other BHJ OSC and for inducing nanoscale phase separation.

5. Experimental Section

Materials: HiPCO SWNT and regioregular poly(3-dodecylthiophene-2,5-diyl) (rr-P3DDT) were, respectively, purchased from Unidym Inc. and Sigma–Aldrich. Regioregular poly(3-hexylthiophene-2,5-diyl) (rr-P3HT) was purchased from Rieke Metals while [6,6]-phenyl-C_{61}-butyric acid methyl ester (PCBM) was obtained from Nano-C. All chemicals were used as received without purification.

Sorting of SWNT: The sorting methodology has been reported in our previous publication.[63] A mixture of HiPCO SWNT and P3DDT (weight ratio = 1:1) was dispersed in toluene to make up a total concentration of 0.4 mg mL^{-1}. The suspension was subsequently ultrasonicated (Cole-Parmer Ultrasonic Processor 750 W) in a temperature-controlled cooling bath (≈50 °C) for 30 min at an amplitude level of 70%. Then it was centrifuged (Sorvall RC5C-plus) at 12 °C for 90 min at 17 000 rpm. Only the supernatant, which was free from metallic SWNTs, was collected and used for solar cell device fabrication. Toluene was evaporated from as-sorted solution with a rotary evaporator. The sc-SWNT residue was then redispersed in 1,2-dichlorobenzene (*o*-DCB) in a bath sonicator for 30 min to make up a stock solution with concentration of 1.25 mg mL^{-1}. No formation of *o*-DCB sonopolymer fragments was observed in the sc-SWNT solution after ultrasonic dispersion.[121]

Device Fabrication and Characterization: The active blend solution was prepared from a mixture of rr-P3HT and PCBM in *o*-DCB (rr-P3HT concentration = 25 mg mL^{-1}). The donor:acceptor (D:A) ratio was 10:8 by weight, unless otherwise stated. The concentration of sc-SWNT in the blend solution, which was defined with respect to the total weight of active materials, could be varied by adjusting the amount of nanotube stock solution (1.25 mg mL^{-1}) and *o*-DCB added to dissolve the active materials. The solutions were stirred overnight at 60 °C. The devices were fabricated with the following configuration: ITO/PEDOT:PSS/rr-P3HT:PCBM:sc-SWNT/Ca/Al. Indium tin oxide (ITO)-coated glass substrates (Thin Film Devices Inc.) were sequentially cleaned in ultrasonic bath with detergent (Extran 300), deionized water, acetone, and isopropanol each for 15 min, followed by ultraviolet-ozone (UVO) treatment for 20 min. A 25 nm thick PEDOT:PSS (Clevios Al 4083, H. C. Stark) was spin-coated at 4000 rpm for 45 s and was immediately dried at 140 °C for 10 min. The substrates were brought into N_2 glovebox for the deposition of subsequent layers. Prior to the deposition, the blend solutions were ultrasonicated for 30 min to homogenize sc-SWNT dispersion. The active layers were then spin-coated at 800 rpm for 2 min to yield 200 nm thick blend films. No filtration was done on the blend solutions. Afterward, the films were thermally annealed at 150 °C for 20 min. For thermal stability study, the annealing was extended to 5 h and 9 h. The device fabrication was completed with thermally evaporated (10^{-6} Torr) cathode consisting of 7 nm of Ca and 100 nm of Al. The device active area was 0.1 cm^2. All device characterizations were performed in N_2 glove box. The current density–voltage (*J*–*V*) characteristics were recorded both in the dark and under AM1.5G illumination at 100 mW cm^{-2} (91160 300 W Oriel solar simulator) with Keithley 2400 source meter. The light intensity was calibrated with an NREL-calibrated Si photodiode with KG5 a filter. EQE measurement was done with a lock-in amplifier (SR830, Stanford Research Systems) under monochromatic light illumination. The EQE was obtained by measuring the ratio of the device photocurrent to the current generated by a standard photodiode under zero-bias voltage as a function of wavelength (400–800 nm).

SWNT and Blend Characterizations: UV–Vis–NIR and UV–Vis absorption spectroscopy measurements were carried out with a UV–Vis–NIR spectrophotometer (Cary 6000i, Varian Inc.) on SWNT and polymer

blend films, respectively. The absorption spectra of the sorted sc-SWNT solution were measured without any dilution with toluene as the background while the solid-state samples were prepared by spin-coating of as-sorted nanotube and active blend solutions on glass substrates. PL spectra of the blend films were recorded with a spectrofluorometer (FL3-21HR, HORIBA Jovin Yvon GmbH). The spin-coating conditions for the blend films were identical to those used for device fabrication. Tapping-mode AFM was performed with a Multimode Nanoscope III with Extender Electronics Module (Veeco Instruments Inc.) on spin-coated Si substrates. Thickness measurement was done with a surface profilometer (Dektak 150, Veeco Instruments Inc.). Grazing incidence X-ray diffraction (GIXRD) measurements were carried out at the Stanford Synchrotron Radiation Lightsource (SSRL, USA) using beam line 11-3 with a photon wavelength of 0.09758 nm. The diffraction intensity was detected on a 2D image plate (MAR-345). The beam size was 50 μm × 150 μm and the incidence angle was in the range of 0.10°–0.12° to optimize the signal-to-noise ratio. In situ heating GIXRD studies of the polymer blends were performed in a custom-built chamber.[74] To prevent sample degradation and to reduce the background noise from air scattering, helium was flowed into the chamber at 200 cm^3 min^{-1}. The heating rate used in the study was 10 °C min^{-1}. Collection time ranges from 2 to 3 min depending on the diffraction strength of the blend films. The samples for GIXRD study were prepared by spin-coating blend solutions onto Si substrates.

Supporting Information

Supporting Information is available from the Wiley Online Library or from the author.

Acknowledgements

The authors thank Eric Verploegen (SSRL) for his help with GIXRD measurements and Prof. Michael McGehee (Stanford University) for allowing the use of his facilities for device fabrication. T.S. thanks Ian Ferguson Postgraduate Fellowship for support.

Received: August 4, 2015
Revised: October 14, 2015
Published online: November 20, 2015

[1] C. J. Brabec, S. Gowrisanker, J. J. M. Halls, D. Laird, S. Jia, S. P. Williams, *Adv. Mater.* **2010**, *22*, 3839.
[2] G. Li, R. Zhu, Y. Yang, *Nat. Photonics* **2012**, *6*, 153.
[3] N. Yeh, P. Yeh, *Renewable Sustainable Energy Rev.* **2013**, *21*, 421.
[4] Z. He, C. Zhong, S. Su, M. Xu, H. Wu, Y. Cao, *Nat. Photonics* **2012**, *6*, 591.
[5] J. You, L. Dou, K. Yoshimura, T. Kato, K. Ohya, T. Moriarty, K. Emery, C.-C. Chen, J. Gao, G. Li, Y. Yang, *Nat. Commun.* **2013**, *4*, 1446.
[6] W. Ma, C. Yang, X. Gong, K. Lee, A. J. Heeger, *Adv. Funct. Mater.* **2005**, *15*, 1617.
[7] G. Li, V. Shrotriya, J. Huang, Y. Yao, T. Moriarty, K. Emery, Y. Yang, *Nat. Mater.* **2005**, *4*, 864.
[8] Y. Yao, J. Hou, Z. Xu, G. Li, Y. Yang, *Adv. Funct. Mater.* **2008**, *18*, 1783.
[9] T. Salim, L. H. Wong, B. Bräuer, R. Kukreja, Y. L. Foo, Z. Bao, Y. M. Lam, *J. Mater. Chem.* **2011**, *21*, 242.
[10] P. Cheng, L. Ye, X. Zhao, J. Hou, Y. Li, X. Zhan, *Energy Environ. Sci.* **2014**, *7*, 1351.
[11] S. Berson, R. De Bettignies, S. Bailly, S. Guillerez, *Adv. Funct. Mater.* **2007**, *17*, 1377.
[12] T. Salim, S. Sun, L. H. Wong, L. Xi, Y. L. Foo, Y. M. Lam, *J. Phys. Chem. C* **2010**, *114*, 9459.
[13] P. Cheng, X. Zhan, *Mater. Horiz.* **2015**, *2*, 462.
[14] T. Ameri, P. Khoram, J. Min, C. J. Brabec, *Adv. Mater.* **2013**, *25*, 4245.
[15] S. Honda, T. Nogami, H. Ohkita, H. Benten, S. Ito, *ACS Appl. Mater. Interfaces* **2009**, *1*, 804.
[16] C. S. Kim, L. L. Tinker, B. F. DiSalle, E. D. Gomez, S. Lee, S. Bernhard, Y.-L. Loo, *Adv. Mater.* **2009**, *21*, 3110.
[17] P. Cheng, Y. Li, X. Zhan, *Energy Environ. Sci.* **2014**, *7*, 2005.
[18] S. Berson, R. de Bettignies, S. Bailly, S. Guillerez, B. Jousselme, *Adv. Funct. Mater.* **2007**, *17*, 3363.
[19] E. Kymakis, N. Kornilios, E. Koudoumas, *J. Phys. D: Appl. Phys.* **2008**, *41*, 165110.
[20] H. Derbal-Habak, C. Bergeret, J. Cousseau, J. M. Nunzi, *Sol. Energy Mater. Sol. Cells* **2011**, *95*, S53.
[21] Z. Liu, D. He, Y. Wang, H. Wu, J. Wang, H. Wang, *Sol. Energy Mater. Sol. Cells* **2010**, *94*, 2148.
[22] J. M. Lee, J. S. Park, S. H. Lee, H. Kim, S. Yoo, S. O. Kim, *Adv. Mater.* **2011**, *23*, 629.
[23] M.-C. Wu, Y.-Y. Lin, S. Chen, H.-C. Liao, Y.-J. Wu, C.-W. Chen, Y.-F. Chen, W.-F. Su, *Chem. Phys. Lett.* **2009**, *468*, 64.
[24] N. A. Nismy, A. A. D. T. Adikaari, S. R. P. Silva, *Appl. Phys. Lett.* **2010**, *97*, 033105.
[25] P. M. Ajayan, J. M. Tour, *Nature* **2007**, *447*, 1066.
[26] M. F. L. De Volder, S. H. Tawfick, R. H. Baughman, A. J. Hart, *Science* **2013**, *339*, 535.
[27] S. Park, M. Vosguerichian, Z. Bao, *Nanoscale* **2013**, *5*, 1727.
[28] S.-Y. Park, W.-D. Kim, D.-G. Kim, J.-K. Kim, Y.-S. Jeong, J. H. Kim, J. K. Lee, S. H. Kim, J.-W. Kang, *Sol. Energy Mater. Sol. Cells* **2010**, *94*, 750.
[29] K. M. Kim, K. W. Lee, A. Moujoud, S. H. Oh, K. Y. Heo, H. J. Kim, *Jpn. J. Appl. Phys.* **2010**, *49*, 111602.
[30] M. M. Stylianakis, J. A. Mikroyannidis, E. Kymakis, *Sol. Energy Mater. Sol. Cells* **2010**, *94*, 267.
[31] V. C. Tung, J.-H. Huang, J. Kim, A. J. Smith, C.-W. Chu, J. Huang, *Energy Environ. Sci.* **2012**, *5*, 7810.
[32] M. P. Ramuz, M. Vosgueritchian, P. Wei, C. Wang, Y. Gao, Y. Wu, Y. Chen, Z. Bao, *ACS Nano* **2012**, *6*, 10384.
[33] M. Bernardi, J. Lohrman, P. V. Kumar, A. Kirkeminde, N. Ferralis, J. C. Grossman, S. Ren, *ACS Nano* **2012**, *6*, 8896.
[34] S. Cataldo, P. Salice, E. Menna, B. Pignataro, *Energy Environ. Sci.* **2012**, *5*, 5919.
[35] G. Centi, S. Perathoner, *ChemSusChem* **2011**, *4*, 913.
[36] G. V. Dubacheva, C.-K. Liang, D. M. Bassani, *Coord. Chem. Rev.* **2012**, *256*, 2628.
[37] T. Song, S.-T. Lee, B. Sun, *J. Mater. Chem.* **2012**, *22*, 4216.
[38] L. Liu, W. E. Stanchina, G. Li, *Appl. Phys. Lett.* **2009**, *94*, 233309.
[39] J. M. Holt, A. J. Ferguson, N. Kopidakis, B. A. Larsen, J. Bult, G. Rumbles, J. L. Blackburn, *Nano Lett.* **2010**, *10*, 4627.
[40] W. L. Abeygunasekara, P. Hiralal, L. Samaranayake, C.-T. Chien, A. Kumar, A. J. Flewitt, V. Karunaratne, G. A. J. Amaratunga, *Appl. Phys. Lett.* **2015**, *106*, 123305.
[41] J. U. Lee, J. W. Jung, T. Emrick, T. P. Russell, W. H. Jo, *J. Mater. Chem.* **2010**, *20*, 3287.
[42] Z. Sun, K. Xiao, J. K. Keum, X. Yu, K. Hong, J. Browning, I. N. Ivanov, J. Chen, J. Alonzo, D. Li, B. G. Sumpter, E. A. Payzant, C. M. Rouleau, D. B. Geohegan, *Adv. Mater.* **2011**, *23*, 5529.
[43] K. Sivula, Z. T. Ball, N. Watanabe, J. M. J. Fréchet, *Adv. Mater.* **2006**, *18*, 206.
[44] C. Yang, J. K. Lee, A. J. Heeger, F. Wudl, *J. Mater. Chem.* **2009**, *19*, 5416.
[45] J. U. Lee, J. W. Jung, T. Emrick, T. P. Russell, W. H. Jo, *Nanotechnology* **2010**, *21*, 105201.
[46] S. Bertho, B. Campo, F. Piersimoni, D. Spoltore, J. D'Haen, L. Lutsen, W. Maes, D. Vanderzande, J. Manca, *Sol. Energy Mater. Sol. Cells* **2013**, *110*, 69.

[47] B. J. Kim, Y. Miyamoto, B. Ma, J. M. J. Fréchet, *Adv. Funct. Mater.* **2009**, *19*, 2273.
[48] S. Miyanishi, K. Tajima, K. Hashimoto, *Macromolecules* **2009**, *42*, 1610.
[49] S. Khiev, L. Derue, G. Ayenew, H. Medlej, R. Brown, L. Rubatat, R. C. Hiorns, G. Wantz, C. Dagron-Lartigau, *Polym. Chem.* **2013**, *4*, 4145.
[50] H. J. Kim, A. R. Han, C.-H. Cho, H. Kang, H.-H. Cho, M. Y. Lee, J. M. J. Fréchet, J. H. Oh, B. J. Kim, *Chem. Mater.* **2011**, *24*, 215.
[51] Y.-J. Cheng, C.-H. Hsieh, P.-J. Li, C.-S. Hsu, *Adv. Funct. Mater.* **2011**, *21*, 1723.
[52] M. Drees, H. Hoppe, C. Winder, H. Neugebauer, N. S. Sariciftci, W. Schwinger, F. Schaffler, C. Topf, M. C. Scharber, Z. Zhu, R. Gaudiana, *J. Mater. Chem.* **2005**, *15*, 5158.
[53] S.-O. Kim, D. Sung Chung, H. Cha, J. Wan Jang, Y.-H. Kim, J.-W. Kang, Y.-S. Jeong, C. E. Park, S.-K. Kwon, *Sol. Energy Mater. Sol. Cells* **2011**, *95*, 432.
[54] C.-Z. Li, S.-C. Chien, H.-L. Yip, C.-C. Chueh, F.-C. Chen, Y. Matsuo, E. Nakamura, A. K. Y. Jen, *Chem. Commun.* **2011**, *47*, 10082.
[55] Y. Zhang, H.-L. Yip, O. Acton, S. K. Hau, F. Huang, A. K. Y. Jen, *Chem. Mater.* **2009**, *21*, 2598.
[56] H.-W. Liu, D.-Y. Chang, W.-Y. Chiu, S.-P. Rwei, L. Wang, *J. Mater. Chem.* **2012**, *22*, 15586.
[57] C.-Y. Chen, C.-S. Tsao, Y.-C. Huang, H.-W. Liu, W.-Y. Chiu, C.-M. Chuang, U. S. Jeng, C.-J. Su, W.-R. Wu, W.-F. Su, L. Wang, *Nanoscale* **2013**, *5*, 7629.
[58] K. Sivula, C. K. Luscombe, B. C. Thompson, J. M. J. Fréchet, *J. Am. Chem. Soc.* **2006**, *128*, 13988.
[59] C. H. Woo, B. C. Thompson, B. J. Kim, M. F. Toney, J. M. J. Fréchet, *J. Am. Chem. Soc.* **2008**, *130*, 16324.
[60] Z. Zhou, X. Chen, S. Holdcroft, *J. Am. Chem. Soc.* **2008**, *130*, 11711.
[61] S. Bertho, G. Janssen, T. J. Cleij, B. Conings, W. Moons, A. Gadisa, J. D'Haen, E. Goovaerts, L. Lutsen, J. Manca, D. Vanderzande, *Sol. Energy Mater. Sol. Cells* **2008**, *92*, 753.
[62] J. Vandenbergh, B. Conings, S. Bertho, J. Kesters, D. Spoltore, S. Esiner, J. Zhao, G. Van Assche, M. M. Wienk, W. Maes, L. Lutsen, B. Van Mele, R. A. J. Janssen, J. Manca, D. J. M. Vanderzande, *Macromolecules* **2011**, *44*, 8470.
[63] H. W. Lee, Y. Yoon, S. Park, J. H. Oh, S. Hong, L. S. Liyanage, H. Wang, S. Morishita, N. Patil, Y. J. Park, J. J. Park, A. Spakowitz, G. Galli, F. Gygi, P. H. S. Wong, J. B. H. Tok, J. M. Kim, Z. Bao, *Nat. Commun.* **2011**, *2*, 541.
[64] M. T. Dang, L. Hirsch, G. Wantz, *Adv. Mater.* **2011**, *23*, 3597.
[65] M. T. Dang, L. Hirsch, G. Wantz, J. D. Wuest, *Chem. Rev.* **2013**, *113*, 3734.
[66] T. Schuettfort, A. Nish, R. J. Nicholas, *Nano Lett.* **2009**, *9*, 3871.
[67] H. Yan, D. Li, K. Lu, X. Zhu, Y. Zhang, Y. Yang, Z. Wei, *Phys. Chem. Chem. Phys.* **2012**, *14*, 15127.
[68] T. Schuettfort, H. J. Snaith, A. Nish, R. J. Nicholas, *Nanotechnology* **2010**, *21*, 025201.
[69] S. D. Stranks, C. Weisspfennig, P. Parkinson, M. B. Johnston, L. M. Herz, R. J. Nicholas, *Nano Lett.* **2010**, *11*, 66.
[70] J. Tsukamoto, J. Mata, *Jpn. J. Appl. Phys.* **2004**, *43*, L214.
[71] J. Geng, T. Zeng, *J. Am. Chem. Soc.* **2006**, *128*, 16827.
[72] M. Bernardi, M. Giulianini, J. C. Grossman, *ACS Nano* **2010**, *4*, 6599.
[73] R. K. Singh, J. Kumar, A. Kumar, V. Kumar, R. Kant, R. Singh, *Sol. Energy Mater. Sol. Cells* **2010**, *94*, 2386.
[74] E. Verploegen, R. Mondal, C. J. Bettinger, S. Sok, M. F. Toney, Z. Bao, *Adv. Funct. Mater.* **2010**, *20*, 3519.
[75] K. Kanemoto, T. Sudo, I. Akai, H. Hashimoto, T. Karasawa, Y. Aso, T. Otsubo, *Phys. Rev. B* **2006**, *73*, 235203.
[76] J. Piris, T. E. Dykstra, A. A. Bakulin, P. H. M. V. Loosdrecht, W. Knulst, M. T. Trinh, J. M. Schins, L. D. A. Siebbeles, *J. Phys. Chem. C* **2009**, *113*, 14500.
[77] N. J. Alley, K.-S. Liao, E. Andreoli, S. Dias, E. P. Dillon, A. W. Orbaek, A. R. Barron, H. J. Byrne, S. A. Curran, *Synth. Met.* **2012**, *162*, 95.
[78] U. Zhokhavets, T. Erb, H. Hoppe, G. Gobsch, N. S. Sariciftci, *Thin Solid Films* **2006**, *496*, 679.
[79] A. L. Ayzner, C. J. Tassone, S. H. Tolbert, B. J. Schwartz, *J. Phys. Chem. C* **2009**, *113*, 20050.
[80] H.-Y. Chen, H. Yang, G. Yang, S. Sista, R. Zadoyan, G. Li, Y. Yang, *J. Phys. Chem. C* **2009**, *113*, 7946.
[81] A. J. Pearson, T. Wang, R. A. L. Jones, D. G. Lidzey, P. A. Staniec, P. E. Hopkinson, A. M. Donald, *Macromolecules* **2012**, *45*, 1499.
[82] B. Xu, S. Holdcroft, *Macromolecules* **1993**, *26*, 4457.
[83] Y. Kim, S. Cook, S. M. Tuladhar, S. A. Choulis, J. Nelson, J. R. Durrant, D. D. C. Bradley, M. Giles, I. McCulloch, C.-S. Ha, M. Ree, *Nat. Mater.* **2006**, *5*, 203.
[84] J. Arranz-Andrés, W. J. Blau, *Carbon* **2008**, *46*, 2067.
[85] J. Kumar, R. K. Singh, V. Kumar, R. C. Rastogi, R. Singh, *Diamond Relat. Mater.* **2007**, *16*, 446.
[86] R. Radbeh, E. Parbaile, M. Chakaroun, B. Ratier, M. Aldissi, A. Moliton, *Polym. Int.* **2010**, *59*, 1514.
[87] Y. Kanai, J. C. Grossman, *Nano Lett.* **2008**, *8*, 908.
[88] A. Pfau, A. Janke, W. Heckmann, *Surf. Interface Anal.* **1999**, *27*, 410.
[89] S. H. Park, A. Roy, S. Beaupre, S. Cho, N. Coates, J. S. Moon, D. Moses, M. Leclerc, K. Lee, A. J. Heeger, *Nat. Photonics* **2009**, *3*, 302.
[90] J. Zhou, Y. Zuo, X. Wan, G. Long, Q. Zhang, W. Ni, Y. Liu, Z. Li, G. He, C. Li, B. Kan, M. Li, Y. Chen, *J. Am. Chem. Soc.* **2013**, *135*, 8484.
[91] P. N. Murgatroyd, *J. Phys. D: Appl. Phys.* **1970**, *3*, 151.
[92] J.-H. Tsai, Y.-C. Lai, T. Higashihara, C.-J. Lin, M. Ueda, W.-C. Chen, *Macromolecules* **2010**, *43*, 6085.
[93] H. Xin, O. G. Reid, G. Ren, F. S. Kim, D. S. Ginger, S. A. Jenekhe, *ACS Nano* **2010**, *4*, 1861.
[94] R. Mauer, M. Kastler, F. Laquai, *Adv. Funct. Mater.* **2010**, *20*, 2085.
[95] L. S. Liyanage, H. Lee, N. Patil, S. Park, S. Mitra, Z. Bao, H.-S. P. Wong, *ACS Nano* **2011**, *6*, 451.
[96] K. Kim, J. W. Shin, Y. B. Lee, M. Y. Cho, S. H. Lee, D. H. Park, D. K. Jang, C. J. Lee, J. Joo, *ACS Nano* **2010**, *4*, 4197.
[97] F. Lan, G. Li, *Nano Lett.* **2013**, *13*, 2086.
[98] E. Kymakis, P. Servati, P. Tzanetakis, E. Koudoumas, N. Kornilios, I. Rompogiannakis, Y. Franghiadakis, G. A. J. Amaratunga, *Nanotechnology* **2007**, *18*, 435702.
[99] N. M. Dissanayake, Z. Zhong, *Nano Lett.* **2010**, *11*, 286.
[100] A. T. Mallajosyula, S. S. K. Iyer, B. Mazhari, *J. Appl. Phys.* **2010**, *108*, 094902.
[101] A. T. Mallajosyula, S. S. K. Iyer, B. Mazhari, *Curr. Appl. Phys.* **2013**, *13*, 677.
[102] S. S. Lee, C. S. Kim, E. D. Gomez, B. Purushothaman, M. F. Toney, C. Wang, A. Hexemer, J. E. Anthony, Y.-L. Loo, *Adv. Mater.* **2009**, *21*, 3605.
[103] W. C. Tsoi, S. J. Spencer, L. Yang, A. M. Ballantyne, P. G. Nicholson, A. Turnbull, A. G. Shard, C. E. Murphy, D. D. C. Bradley, J. Nelson, J.-S. Kim, *Macromolecules* **2011**, *44*, 2944.
[104] J.-H. Kim, J. H. Park, J. H. Lee, J. S. Kim, M. Sim, C. Shim, K. Cho, *J. Mater. Chem.* **2010**, *20*, 7398.
[105] M. Reyes-Reyes, K. Kim, J. Dewald, R. López-Sandoval, A. Avadhanula, S. Curran, D. L. Carroll, *Org. Lett.* **2005**, *7*, 5749.
[106] M. Abbas, N. Tekin, *Appl. Phys. Lett.* **2012**, *101*, 073302.
[107] S. Chaudhary, H. Lu, A. M. Müller, C. J. Bardeen, M. Ozkan, *Nano Lett.* **2007**, *7*, 1973.
[108] J. J. M. Halls, K. Pichler, R. H. Friend, S. C. Moratti, A. B. Holmes, *Appl. Phys. Lett.* **1996**, *68*, 3120.

[109] M. Theander, A. Yartsev, D. Zigmantas, V. Sundström, W. Mammo, M. R. Andersson, O. Inganäs, *Phys. Rev. B* **2000**, *61*, 12957.
[110] A. Haugeneder, M. Neges, C. Kallinger, W. Spirkl, U. Lemmer, J. Feldmann, U. Scherf, E. Harth, A. Gügel, K. Müllen, *Phys. Rev. B* **1999**, *59*, 15346.
[111] H. Wang, H.-Y. Wang, B.-R. Gao, L. Wang, Z.-Y. Yang, X.-B. Du, Q.-D. Chen, J.-F. Song, H.-B. Sun, *Nanoscale* **2011**, *3*, 2280.
[112] S. Cook, A. Furube, R. Katoh, L. Han, *Chem. Phys. Lett.* **2009**, *478*, 33.
[113] G. F. Burkhard, E. T. Hoke, S. R. Scully, M. D. McGehee, *Nano Lett.* **2009**, *9*, 4037.
[114] E. Kymakis, G. A. J. Amaratunga, *Appl. Phys. Lett.* **2002**, *80*, 112.
[115] C. Li, Y. Chen, Y. Wang, Z. Iqbal, M. Chhowalla, S. Mitra, *J. Mater. Chem.* **2007**, *17*, 2406.
[116] J. Geng, B.-S. Kong, S. B. Yang, S. C. Youn, S. Park, T. Joo, H.-T. Jung, *Adv. Funct. Mater.* **2008**, *18*, 2659.
[117] N. A. Nismy, K. D. G. I. Jayawardena, A. A. D. T. Adikaari, S. R. P. Silva, *Adv. Mater.* **2011**, *23*, 3796.
[118] X. Zhou, J.-Y. Park, S. Huang, J. Liu, P. L. McEuen, *Phys. Rev. Lett.* **2005**, *95*, 146805.
[119] T. Durkop, T. Brintlinger, M. S. Fuhrer, *AIP Conf. Proc.* **2002**, *633*, 242.
[120] H. Wang, J. Mei, P. Liu, K. Schmidt, G. Jiménez-Osés, S. Osuna, L. Fang, C. J. Tassone, A. P. Zoombelt, A. N. Sokolov, K. N. Houk, M. F. Toney, Z. Bao, *ACS Nano* **2013**, *7*, 2659.
[121] S. Niyogi, M. A. Hamon, D. E. Perea, C. B. Kang, B. Zhao, S. K. Pal, A. E. Wyant, M. E. Itkis, R. C. Haddon, *J. Phys. Chem. B* **2003**, *107*, 8799.